Materials Chemistry and Physics 217 (2018) 403–411

Contents lists available at ScienceDirect

Materials Chemistry and Physics

journal homepage: www.elsevier.com/locate/matchemphys

Spectroscopic and TD-DFT investigations of 4-{[(2-amino-6-methylchromon-3-yl) methylidene]amino}-6-methyl-3-thioxo-3,4-dihydro-1,2,4-triazin-5(2*H*)-one, and its application for photovoltaic devices

Shimaa Abdel Halim[a], Magdy A. Ibrahim[a], N. Roushdy[b], A.A.M. Farag[c,d,*], Yassin Gabr[a], Sara Said[a]

[a] Department of Chemistry, Faculty of Education, Ain Shams University, Heliopolis, 11757, Cairo, Egypt
[b] Electronics Materials Dep. Advanced Technology & New Materials Research Inst., City of Scientific Research & Technological Applications (SRTA-City), New Borg El-Arab City, P.O. Box: 21934, Alexandria, Egypt
[c] Physics Department, Faculty of Science and Arts, Jouf University, Jouf, Saudi Arabia
[d] Thin Film Laboratory, Physics Department, Faculty of Education, Ain Shams University, Heliopolis, 11757, Cairo, Egypt

HIGHLIGHTS

- The novel 4-amino-6-methyl-3-thioxo-3,4-dihydro-1,2,4-triazin-5(2H)-one structure was efficiently synthesized.
- The electronic structure and electronic absorption spectra of the structure were deduced.
- TD-DFT calculation and optimized geometry at B3LYP/6-311G (p,d) were explored.
- The dispersion parameters of the film were extracted using single oscillator model.

GRAPHICAL ABSTRACT

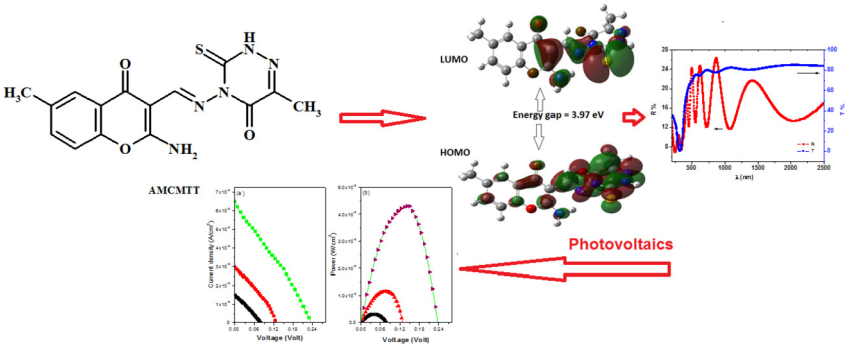

ARTICLE INFO

Keywords:
Chromones
Ring opening ring closure
TD-DFT
Single oscillator model
Photovoltaic properties

ABSTRACT

Chemical transformation of 6-methylchromone-3-carbonitrile (**1**) with 4-amino-6-methyl-3-thioxo-3,4-dihydro-1,2,4-triazin-5(2*H*)-one (**2**) produced the novel 4-{(2-amino-6-methylchromon-3-yr)methylidene]amino}-6-methyl-3-thioxo-3,4-dihydro-1,2,4-triazin-5(2*H*)-one (**AMCMTT**). Essential computations were done by the DFT-calculation at B3LYP/6-311G (d,p) geometry to extract the electrostatic potential, electron density, and other related calculations. Rod-like structure morphology was obtained for **AMCMTT** using the scanning electron microscopy with mean sizes of 210 nm, extracted by the particle size analyzer. The fundamental absorption and dispersion parameters were determined. Two direct and allowed optical band gaps were extracted from the optical absorption edges with values of 1.04 and 2.05 eV, for the onset and fundamental gaps, respectively. The dispersion parameters of the films were extracted based on the single-oscillator model utilizing the well-known Wemple-DiDomenico relationship. The diode and photovoltaic properties of the **AMCMTT**-based heterojunction were investigated using the results of current density-voltage measurements.

* Corresponding author. Thin Film Laboratory, Physics Department, Faculty of Education, Ain Shams University, Heliopolis, 11757, Cairo, Egypt.
E-mail address: alaafaragg@gmail.com (A.A.M. Farag).

https://doi.org/10.1016/j.matchemphys.2018.06.067
Received 2 February 2018; Received in revised form 25 May 2018; Accepted 25 June 2018
Available online 27 June 2018

1. Introduction

Chromones are a set of normally existing compounds that are widespread in nature, particularly in plants [1]. Recently, the chemistry of chromones have been generally investigated and widely explored. Specific consideration has been given to the blend of chromones, since their utilizations and applications in most recent years [2–8]. The science of chromone-3-carbonitriles has been created since the mid-1970s after the basic and helpful Vilsmeier-Haack technique was proposed for the amalgamation of 3-formylchromones from 2-hydroxyacetophenones, DMF and $POCl_3$ [9]. The presentation of the electron-withdrawing CN group at the 3-position of the chromone framework changes significantly the reactivity of the pyrone ring concerning nucleophiles and gives a wide manufacturing capability of chromone-3-carbonitriles [10–13].

The main objective of the present work is to study the reactivity of 6-methylchromone-3-carbonitrile (**1**) [14] towards 4-amino-6-methyl-3-thioxo-3,4-dihydro-1,2,4-triazin-5(2H)-one (2) [15]. Differential function theory (DFT) calculation can be used to investigate the optimized geometries of the synthesized **AMCMTT**. Moreover, the study of the dipole moment, molecular electrostatic potential contours (MEP, ESP, and ED), atomic charge, FT-IR, equilibrium geometries, simple harmonic vibrational frequencies, the thermochemical parameters, and the energy of the molecule is concerned. In addition, the calculation with aiding time-dependent-DFT (TD-DFT) to give a prediction for the charge transfer and other important characteristics, described in details by Becke [16], is also considered. The optical absorptivity and dispersive properties were examined. Finally, the photovoltaic characteristics of **AMCMTT**-based heterojunction were investigated in a wide range of illumination intensity to obtain the appropriate photovoltaic parameters suitable for optoelectronic application.

2. Experimental

2.1. Preparation and molecular structural characterizations of *AMCMTT*

A refluxed mixture of 6-methylchromone-3-carbonitrile (**1**) (0.56 g, 3 mmol) and 4-amino-6-methyl-3-thioxo-3,4-dihydro-1,2,4-triazin-5(2*H*)-one (**2**) (0.47 g, 3 mmol) in absolute alcohol (20 mL). The yellow crystals obtained during heating were filtered off and crystallized from AcOH/H_2O to give **AMCMTT** as pale yellow crystals, mp 301–302 °C, yield (0.71 g, 69%). IR (KBr, cm^{-1}): 3433, 3273, 3139 (NH_2, NH), 3057 ($CH_{arom.}$), 1693 (C=$O_{triazine}$), 1652 (C=$O_{\gamma\text{-pyrone}}$), 1612 (C=N), 1571 (C=C), and 1173 (C=S). ^{1}H NMR (DMSO-d_6, δ, 400 MHz): 2.16 (s, 3H, $CH_{3\ triazine}$), 2.42 (CH_{3} benzo), 7.35 (d, 1H, J = 8.4 Hz, H-8), 7.52 (d, 1H, J = 8.4 Hz, H-7), 7.79 (s, 1H, H-5), 8.92 (s, 1H, CH=N), 9.45 (bs, 1H, NH exchangeable with D_2O), 9.68 (bs, 1H, NH exchangeable with D_2O), 13.59 (bs, 1H, $NH_{triazine}$ exchangeable with D_2O). ^{13}C NMR (DMSO-d_6, δ, 100 MHz): 17.3 ($CH_{3\ triazine}$), 20.8 ($CH_{3\ benzo}$), 92.6 (C-$3_{chromone}$), 117.1 (C-$8_{chromone}$), 121.3 (C-4a), 125.4 (C-$5_{chromone}$), 135.1 (C-$6_{chromone}$), 135.2 (C-$7_{chromone}$), 147.9 (C-$6_{triazine}$), 150.9 (C-8a), 151.5 (CH=N), 164.5 (C-$5_{triazine}$ as C=O), 166.5 (C-$4_{chromone}$ as C=O), 171.8 (C-2 $_{chromone}$), 174.3 (C-$3_{triazine}$ as C=S). Anal. Calcd for $C_{15}H_{13}N_5O_3S$ (343.36): C, 52.47; H, 3.82; N, 20.40; S, 9.34%. Found: C, 52.30; H, 3.75; N, 20.25; S, 9.20%. The instruments used for determining the melting point, infrared spectra, ^{1}H NMR and ^{13}C NMR spectra, Elemental microanalyses and the suitable solvents were described elsewhere by our group work [11–13].

2.2. Computation and methodology

Computations were assessed by utilizing Khon-Sham's DFT method, subjected to the gradient-corrected hybrid density functional B3LYP method [16,17]. For the structure, the 6-311G (p,d) bases set [18] was used for a full geometry optimization using the published function [17] which implemented by Gaussian 09 package [19]. All the produced geometries were done by Gauss View 5.0.9 [20] and/or Chemcraft 1.6 software packages [21].

2.3. Thin film preparation and physical characterizations of *AMCMTT*

Thermal evaporation technique type Edward Auto 306 was used for obtaining a uniform film of **AMCMTT** on a planar corning glasses and single crystalline substrates. This method was appropriate for employing optoelectronic devices applications. The thermal gravimetric analysis was achieved by using Shimadzu-50H thermal analyzer with heating temperature range of 20–1000 °C with the heating rate of 10 °C/min. The topographical characterization of the surface was recognized by JEOL-JSM-636 OLA scanning electron microscope. The thermal stability characterization of the sample was analyzed by using the Shimadzu-50H thermal analyzer. The optical measurements were considered for obtaining the optical gap and other important related parameters using JASCO-570 spectrophotometer. To estimate the characteristics of the **AMCMTT** based heterojunction, current-voltage measurements were done in dark condition. In addition, for optoelectronic measurements, current-voltage characteristics were considered using high impedance Keithly 2635A under various illuminations.

3. Results and discussion

3.1. Molecular structure and reaction confirmation

In the present work, the chemical transformation of 6-methylchromone-3-carbonitrile (**1**) with 4-amino-6-methyl-3-thioxo-3,4-dihydro-1,2,4-triazin-5(2*H*)-one (**2**) in boiling ethanol produced a novel Schiff base (**AMCMTT**) in which 2-amino-6-methylchromone linked 6-methyl-3-thioxo-3,4-dihydro-1,2,4-triazin-5(2*H*)-one through azomethine linkage. The **AMCMTT** was synthesized,as shown in Fig. 1(a), *via* ring opening ring closure reaction of 6-methylchromone-3-carbonitrile (**1**) with the nucleophile used. The reaction may proceed *via* nucleophilic attack of amino group at C-2 position of chromone moiety with concomitant γ–pyrone ring opening leading to intermediate **A**. Nucleophilic addition of hydroxyl group onto the nitrile function afforded iminochromone intermediate **B**, which upon proton transfer yielded the final product 4-{(2-amino-6-methylchromon-3-yl)methylidene]amino}-6-methyl-3-thioxo-3,4 dihydro-1,2,4-triazin-5(2*H*)-one (**AMCMTT**). The structure of **AMCMTT** was deduced from its correct elemental analysis and spectral data. The IR (Fig. 1(b)) showed characteristic absorption bands at 3433, 3273, 3139 (NH_2, NH), 1693 (C=$O_{triazine}$), 1652 (C=$O_{\gamma\text{-pyrone}}$), 1612 (C=N), 1571 (C=C), and 1173 (C=S). The ^{1}H NMR spectrum (not shown here) showed a singlet signals which can be attributed to attributed to $CH_{3\ triazine}$ and $CH_{3\ benzo}$ at δ 2.16 and 2.42, respectively, in addition to singlet signals assigned to H-$5_{chromone}$ and azomethine protons at δ 7.79 and 8.92, respectively. The spectrum also revealed D_2O-exchangeable signals at δ 9.45, 9.68 and 13.59 due to 3NH protons. The ^{13}C NMR spectrum (Fig. 1(c)) agrees well with the assigned structure and the spectrum showed signals at δ 17.3 ($CH_{3\ triazine}$), 20.8 ($CH_{3\ benzo}$), 92.6 (C-$3_{chromone}$), 117.1 (C-$8_{chromone}$), 121.3 (C-4a), 125.4 (C-$5_{chromone}$), 135.1 (C-$6_{chromone}$), 135.2 (C-$7_{chromone}$), 147.9 (C-$6_{triazine}$), 150.9 (C-8a), 151.5 (CH=N), 164.5 (C-$5_{triazine}$ as C=O), 166.5 (C-$4_{chromone}$ as C=O), 171.8 (C-$2_{chromone}$), 174.3 (C-$3_{triazine}$ as C=S). The mass spectrum showed the molecular ion peak at *m/z* 343 with low abundance and the molecule splits into two part which was identified as 6-methylchromone-3-carbonitrile (*m/z*, 201; 39%) and 6-methyl-3-thioxo-3,4-dihydro-1,2,4-triazin-5(2*H*)-one (*m/z*, 143; 72%). The splitting of **AMCMTT** during the fragmentation pattern may attribute to the weak N-N bond force.

3.2. The ground state energy of molecular orbital calculations

The optimized geometries of the compound 4-{(2-amino-6-methylchromon-3-yl)methylidene]amino}-6-methyl-3-thioxo-3,4-dihydro-1,2,4-triazin-5(2*H*)-one (**AMCMTT**) was obtained using the B3LYB/6-311G (p,d) level. The analysis shows that the most stable geometry of the compound is the planar structure, except triazine moiety (where the dihedral angle $N_{23}N_{22}C_{16}O_{20}$ is 8.82° and $H_{31}C_{13}C_{11}C_9$ is 2.01°), are out of the molecular plane. The ionization energy is calculated as 6.17 eV. As well, the electron affinity is found to be 2.20 eV and energy gap, (E_g)

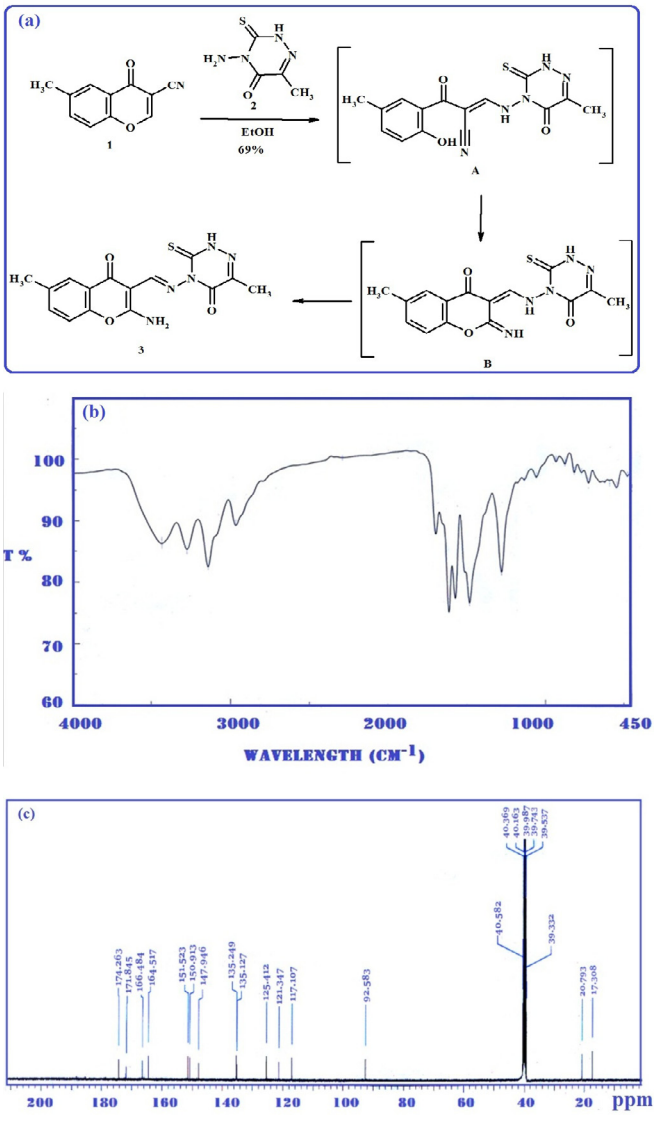

Fig. 1. (a) Formation of the novel AMCMTT, (b) Experimental IR spectrum, and (c) The ^{13}C NMR spectrum of AMCMTT.

is calculated as 3.97 eV as well as the dipole moment (μ) is determined as 3.33 D. The change in the total entropy and the E_{total} energies of the compound were calculated by using B3LYP/6-311G (d,p). Also, the total dipole moment is measured physically and clarifies the capability of the surrounding molecules to react with the considered molecule. The computed HOMO/LUMO molecular orbital of the compound utilizing B3LYP/6-311G (d,p) demonstrates that these orbital decide the way that the particle interacts with different species are the frontier molecular orbital. In addition, the frontier orbital gap E_{gap} assists the physical and chemical characterization of the molecule (Fig. 2).

3.3. Electronic absorption spectra of *AMCMTT*

The electronic spectra of **AMCMTT** in ethanol and chloroform solvents show five bands in the region 200–650 nm (not shown here). These bands will subsequently refer to as λ_1, λ_2, λ_3, λ_4 and λ_5 for 251, 278, 308, 331 and 365 nm, respectively. The first and second absorption maxima at 251 and 278 nm might be attributed to the $\pi \rightarrow \pi^*$ transition. Whereas, λ_3 at 308 nm can be assigned to $\pi - \pi^*$ transitions (K-band) over the whole conjugated system. However, the last two bands at 331 and 365 nm could be assigned to the $n \rightarrow \pi^*$ transition of the amino group and/or the charge transfer (CT) transition through the

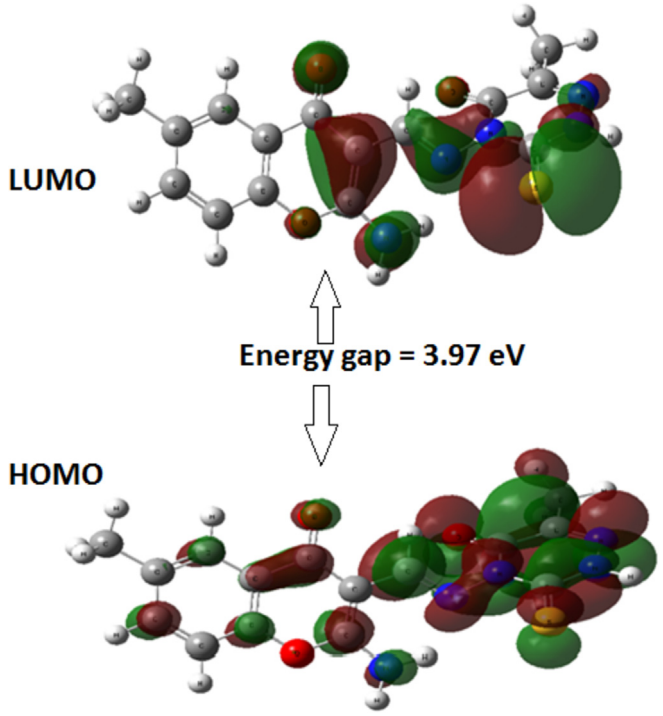

Fig. 2. HOMO and LUMO for 4-{(2-amino-6-methylchromon-3-yl)methylidene] amino}-6-methyl-3-thioxo-3,4-dihydro-1,2,4-triazin-5(2*H*)-one (**AMCMTT**).

molecule, respectively. The charge transfer originates from the chromone ring as a source to the triazine ring. Increasing the solvent polarity ongoing from chloroform to ethanol causes small changes in band positions indicating that the polarity of the excited and ground state is of the same values, that is, solvent independent. UV–vis spectrum of **AMCMTT** shows four essential bands at 365.37 nm, 330.86 nm, 308.40 nm, 278.26 nm, which were attributed to charge transfer, $n \rightarrow \pi^*$ and two $\pi \rightarrow \pi^*$transitions, respectively [22] as reflected from their intensities.

The energized configuration considered in the compound outcomes from the electron excitation of eight highest occupied molecular orbital's $\varphi_{82}{}^{-1}\varphi_{89}$ and the lowest four vacant molecular orbital's $\varphi_{90}{}^{-1}\varphi_{93}$ [23–28]. The first $(\pi\text{-}\pi^*)^1$ state is centered at 365.37 nm in chloroform can be predicted theoretically at 356.87 nm, in agreement with the experimental, and is configurations, namely, $\varphi_{88}{}^{-1}\varphi_{90}$ and $\varphi_{89}{}^{-1}\varphi_{90}$. This band is of CT character from triazine moiety to the chromone moiety. The second $(\pi\text{-}\pi^*)^1$ state is observed at 330.86 nm in chloroform and is predicted theoretically at 323.75 nm and possessed of a blend of six configurations, that is, CT localized and delocalized configurations may be expected. The main contribution of this band is coming from the two configurations $\varphi_{87}{}^{-1}\varphi_{90}$ and $\varphi_{89}{}^{-1}\varphi_{92}$, which is of CT character from triazine moiety to the chromone moiety and delocalized. The third $(\pi\text{-}\pi^*)^1$ state is observed in chloroform at 308.40 nm and predicted theoretically at 305.73 nm. This band is composed of six configurations, namely, $\varphi^{-1}_{82}\varphi_{90}$, $\varphi^{-1}_{84}\varphi_{90}$, $\varphi^{-1}_{86}\varphi_{90}$, $\varphi^{-1}_{89}\varphi_{91}$, $\varphi^{-1}_{89}\varphi_{92}$ and $\varphi^{-1}_{89}\varphi_{93}$. This band is CT character from triazine moiety to the chromone moiety, delocalized and localized bands. The fourth $(\pi\text{-}\pi^*)^1$ state computed theoretically at 276.18 nm and observed in chloroform at 278.26 nm. This state is composed of a mixture of six configurations, that is, CT and delocalized configurations may be expected. The fifth $(\pi, \pi^*)^1$ state computed at 255.44 nm in chloroform, 245.94 nm in ethanol and is computed theoretically at 250.02 nm. This state has a high extremity when contrasted with that of the ground state and hence solvent dependence on band position is expected, which can be attributed to the delocalized and a charge transfer band (CT) from triazine moiety to the chromone moiety. The last one state computed

Table 1
The calculated band maxima and intensities of **AMCMTT** by TD method.

State	Theoretical						Experimental	
	Configuration	Coefficient	Wt. %	λ, nm	f	Type	Polar	Non polar
							λ, nm	λ, nm
I	88–90	0.645	41.60	356.87	0.12	CT	360.56	365.37
II	86–90	0.186	3.46	323.75	0.12	n – π*	326.17	330.86
	86–91	0.166	2.76			n – π*		
	87–90	0.590	34.81			n – π*		
	89–91	0.134	1.80			n – π*		
III	82–90	0.118	1.39	305.73	0.07	n – π*	305.90	308.40
	86–90	0.154	2.37			n – π*		
	89–91	0.541	29.29			n – π*		
	89–92	0.152	2.31			n – π*		
	89–93	0.282	7.95			n – π*		
IV	87–91	0.583	33.99	276.18	0.05	π – π*	270.25	278.26
	88–93	0.190	3.61			π – π*		
V	83–90	0.473	22.37	250.02	0.17	π – π*	245.94	255.44
	85–91	0.160	2.56			π – π*		
	87–92	0.292	8.53			π – π*		
	88–93	0.215	4.62			π – π*		
VI	87–92	0.198	3.92	247.96	0.2	π – π*	240.44	250.61
	87–93	0.542	29.38			π – π*		
	88–92	0.127	1.61			π – π*		
	88–93	0.304	9.24			π – π*		

theoretically, appears at 247.96 nm. Both states are π-π* and can be assigned as a delocalized and localized transition. The calculated band maxima and intensities of **AMCMTT** by TD method are listed in Table 1.

3.4. Molecular electrostatic potential (MEP)

Molecular Electrostatic Potential (MEP) mapping is essential in the investigation of the molecular interactions, forecast of relative locations for nucleophilic and electrophilic assault and predication of various range of macroscopic properties [29].

The calculated MEP is found to increase in the color scheme for the MEP surface, follows the order: red < orange < yellow < green < blue and described in detail elsewhere [28]. The plot of 3D of the well-defined potentials was calculated and observed in Fig. 3. The region of negativity (i.e. blue color) is mainly over the N and O atomic site (can be attributed to the contribution of lone-pair electrons of nitrogen atom), while the positive (i.e. red color) potential portions are surrounded by the hydrogen, sulfur and carbon atoms.

3.5. Thermal analysis characterization

To check the thermal stability of **AMCMTT**, the thermogravimetric analysis in a wide range of temperature by TGA was achieved (as shown in Fig. 4). A well remarkable endothermic peak at ~310 °C in TGA is recorded. Accurately, this endothermic peak can be due to the beginning of adsorption of water molecules on the surface. This broad intense endothermic peak could be related to the melting point of **AMCMTT** or the melting phase.

The TGA analysis of the present **AMCMTT** displays two decay stages. The primary stage (298–320 °C) with an exploratory mass loss of 41.7% refer to the loss of 6-methyl-3-thioxo-3,4-dihydro-1,2,4-triazin-5(2H)- one atom. The second stage inside the temperature range 550–650 °C may be due to the mass loss of the organized **AMCMTT** ligand relating to C=O and C=N, 15.7%, which implies the aggregate loss of 57.4%. The remaining portion of the structure after TGA was portrayed as 42.6%, comparing to an atomic mass of 146 amu. Hence, the TGA information concurring with the proposed structure of the present structure.

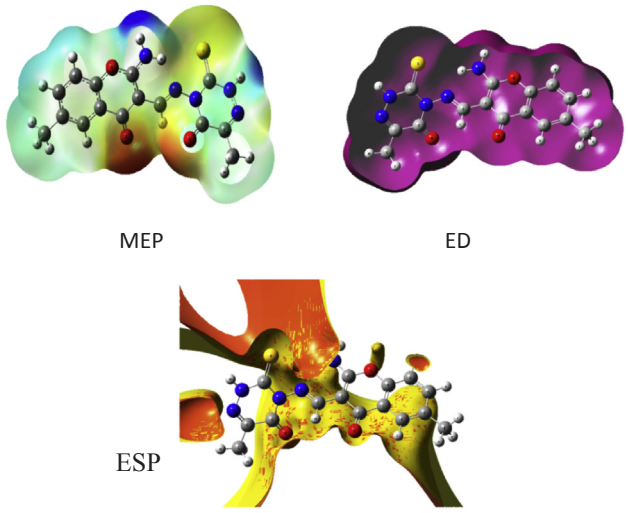

Fig. 3. Molecular surfaces of 4-{(2-amino-6-methylchromon-3-yl)methylidene] amino}-6-methyl-3-thioxo-3,4-dihydro-1,2,4-triazin-5(2*H*)-one (**AMCMTT**) using B3LYP/6-311G (d,p).

3.6. Surface morphology characterization

Fig. 5(a)–(d) shows the SEM images of **AMCMTT** samples with different magnification. A rod-like structure with high regularity in its shape is observed. The crystallite size is considered to be irregular and has wide distribution varying in its values. In addition, some aggregation was also observed as shown in Fig. 5(a)–(d).

Furthermore, the obtained surface morphology gives a high surface area suitable for the probable light absorption for some optoelectronic

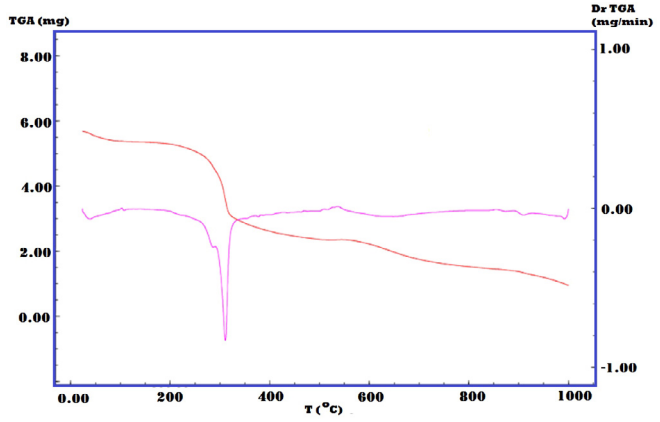

Fig. 4. TGA curve of **AMCMTT** structure.

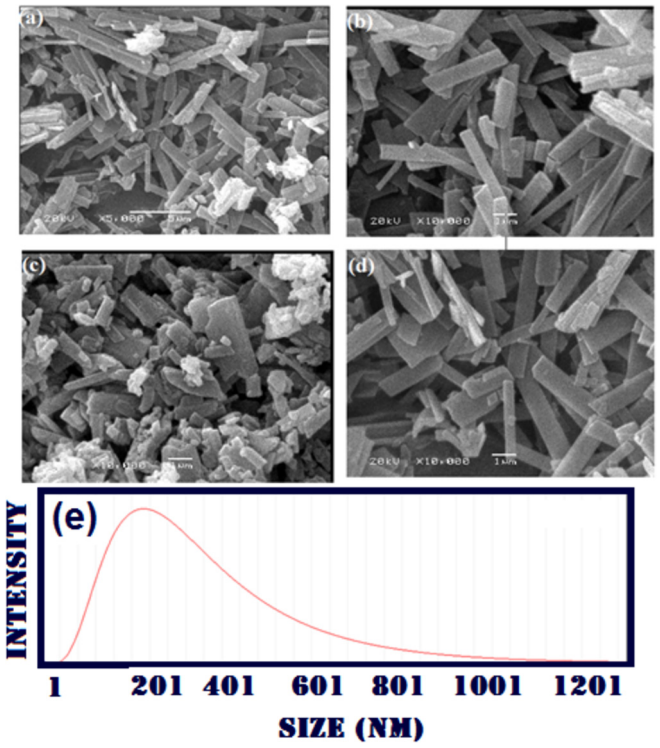

Fig. 5. SEM of different magnifications(a)1000×, (b) 5,000, (c) 10,000 and (d) Particle size analysis of **AMCMTT**.

device applications. The average particle size was estimated by using particle size analyzer and found to be 210 nm as shown in Fig. 5(e).

3.7. Optical characterizations of AMCMTT thin films

The main optical parameters which are considered to be sophisticated for optoelectronic applications were determined from the transmission and reflectance data (Fig. 6). As observed, the optical transmission and reflection display distinguished interference fringes confirming that the **AMCMTT** films are smooth and uniform as discussed by Kaur et al. [30]. Furthermore, the transmission spectrum shows a band edge in the wavelength ~350 nm, after which the transmission approaches to 83% at 2500 nm.

The measured transmittance and reflectance can be used to determine the optical absorption coefficient (α) of the film thickness (d) by the following expression [31]:

$$\alpha = (1/d)\ln(((1-R)^2/2T) + (R^2 + (1-R)^4/4T^2)^{1/2}) \quad (1)$$

According to the band theory, the optical band gap can be estimated from the optical absorption edge using the following relation [32]:

$$(\alpha h\nu) = B(h\nu - E_g)^r \quad (2)$$

Where ***B*** is a characteristic constant and r is an integer identifying the transition type, E_g is the energy gap. The energy band gap can be calculated by extrapolating the straight line fit of the graphical representation of $(\alpha h\nu)^2$ versus hν to x-axis, where $(\alpha h\nu)^2 = 0$ as shown in Fig. 7(a) and (b). The linearity of this presentation confirms that the **AMCMTT** films have a direct band gap and the energy band gaps are found to be 1.04 and 2.05 eV, respectively. The discrepancy between the calculated value of the energy gap utilizing B3LYP/6-311G (d,p) demonstrates (discussed above) and the experimental values might be due to some factors affecting the experimental absorption edge such as the probability of the presence of crystalline bulk imperfection, experimental errors for measuring the film thickness and optical constants [33]. In addition, another reason, due to that the theoretical calculations applied on the single molecule in the gaseous state, neglecting the interactions between molecules, considered in the experimental results [34].

At higher wavelengths (λ > 1000 nm), the value of the refractive index is found to decrease with increasing wavelength, obeying a normal dispersion characteristic to acquire E_d (dispersion energy) and E_0 (the oscillator energy). This can be explained on the basis of single oscillator model and expressed by Wemple and DiDomenico as follows [35]:

$$(n^2 - 1) = \frac{E_d E_0}{E_0^2 - (h\nu)^2} \quad (3)$$

The $(n^2 - 1)^{-1}$ versus $(h\nu)^2$ plot, (Fig. 8(a)), can be fitted to straight line confirming Eq. (3). The obtained values of E_d and E_0 are found to be 3.984 and 2.04 eV, respectively.

In the transparent region, the square of refractive index is represented as a function of square wavelength, λ^2, by the well-known expression using the same symbols expressed in the reference as follows [36]:

$$n^2 = \varepsilon_\infty - \frac{e^2}{4\pi\varepsilon_0 c^2}\frac{N}{m^*}\lambda^2 \quad (4)$$

The n^2 vs. λ^2 plot, (Fig. 8(b)), can be linearly fitted in stratification with Eq. (4). The obtained values of ε_∞ and N/m^* from both the intercept on the vertical axis and the slope of the figure are found to be 2.89 and $6.9 \times 10^{55}\,kg^{-1}m^{-3}$, respectively.

The spectral dependence of dielectric constant provides information about the light propagation and loss in a material and therefore has a significant importance for designing optoelectronic devices [37]. The complex dielectric constant is described by the well-known equation (i.e. $\varepsilon^* = \varepsilon_1 - i\varepsilon_2$ where $\varepsilon_1 = n^2 - k^2$ and $\varepsilon_2 = 2nk$). The experimental value of ε_1 is higher than those for ε_2. Moreover, this behavior shows that there is a probability of some interactions between the incident photons and the charge carriers of the material in the photon energy range [38,39].

3.8. Current density - voltage (J-V) characteristics

The *J-V* characteristics of **AMCMTT**/p-Si heterojunctions are illustrated in Fig. 9(a) in dark and under diverse illumination intensities in the range of 40–100 mW/cm^2. The high rectification characteristics may be attributed to the asymmetric organic/inorganic interfaces in the prepared heterojunction [40]. Accordingly, the forward current is much larger as compared with those for the reverse one under certain applied voltage. In addition, the semi-logarithmic plot of current density-voltage characteristics, shown in Fig. 9(b), are used for extracting the main important parameters of the heterojunction. The values of ideality factor and barrier height of AMCMTT/p-Si heterojunctions can easily be

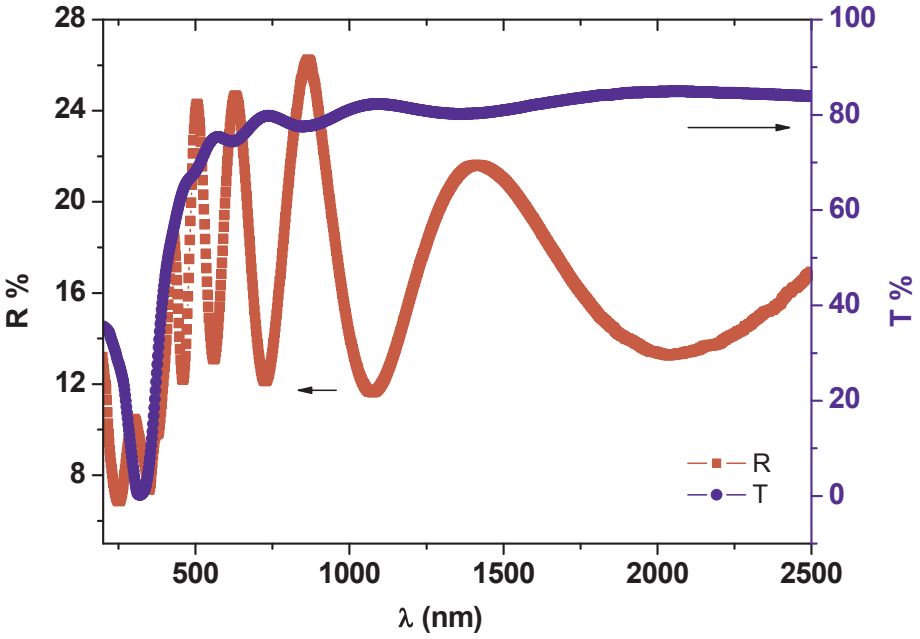

Fig. 6. Spectral dependence of T and R characteristics of **AMCMTT** thin films.

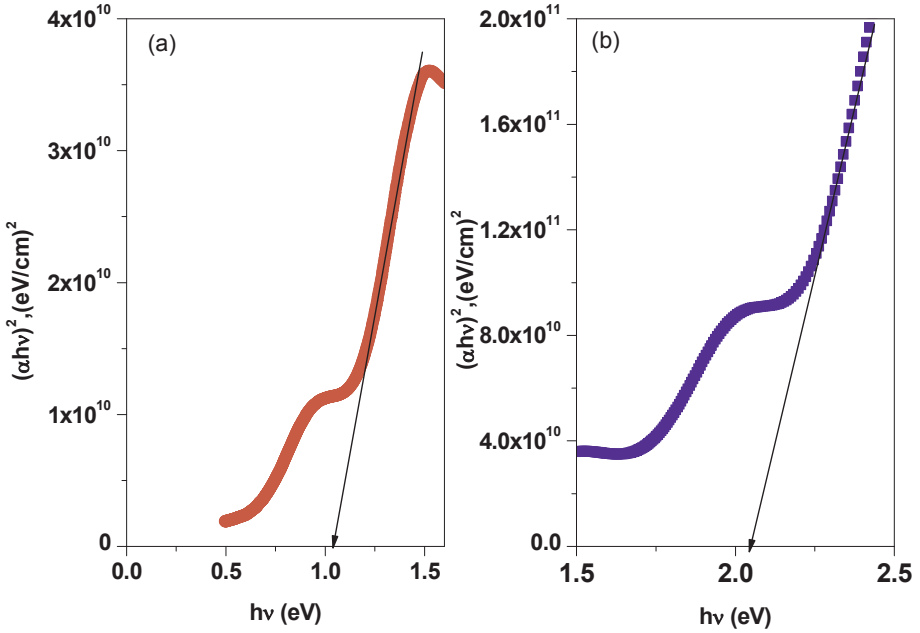

Fig. 7. Plot of $(\alpha h\nu)^2$ vs. $h\nu$ of (a) region I and (b) region II of **AMCMTT** thin films.

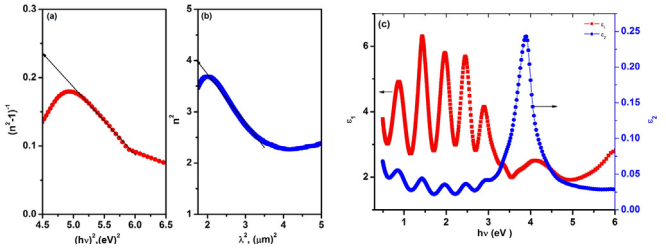

Fig. 8. (a) Plot of $(n^2–1)^{-1}$ vs.$(h\nu)^2$, (b)Plot of n^2 vs. λ^2 and (d) Plot of ε_1 and ε_2 vs. $h\nu$ for **AMCMTT** thin films.

extracted from the plot of *J-V* characteristics using the well-known equation [41] and illustrated in Fig.10. The values of ideality factor are found to decrease with increasing illumination intensity. On the other hand, the values of barrier height increase with increasing illumination intensity. These behaviors can be due to the molecular modulation such as restructuring and reordering of the interface states, generation and recombination processes [41] (see Fig. 10).

The values of series resistance (R_s) and shunt resistance (R_{sh}) can be extracted by using various methods [42–44]. Among them, R_s and R_{sh} are determined from the junction resistance (R_J) against applied bias voltage (V_J) plot (not shown here) by using the data of the current-voltage characteristics (Fig. 9(a)). In this methodology, the series resistance can be obtained from the nearly constant value of the junction resistance at high forward bias, while the shunt resistance can be obtained by the same method at sufficiently reverse bias. The calculated values of both R_s and R_{sh} are tabulated in Table 2 at different illumination intensity.

As observed, the values of R_s and R_{sh} are found to decrease with

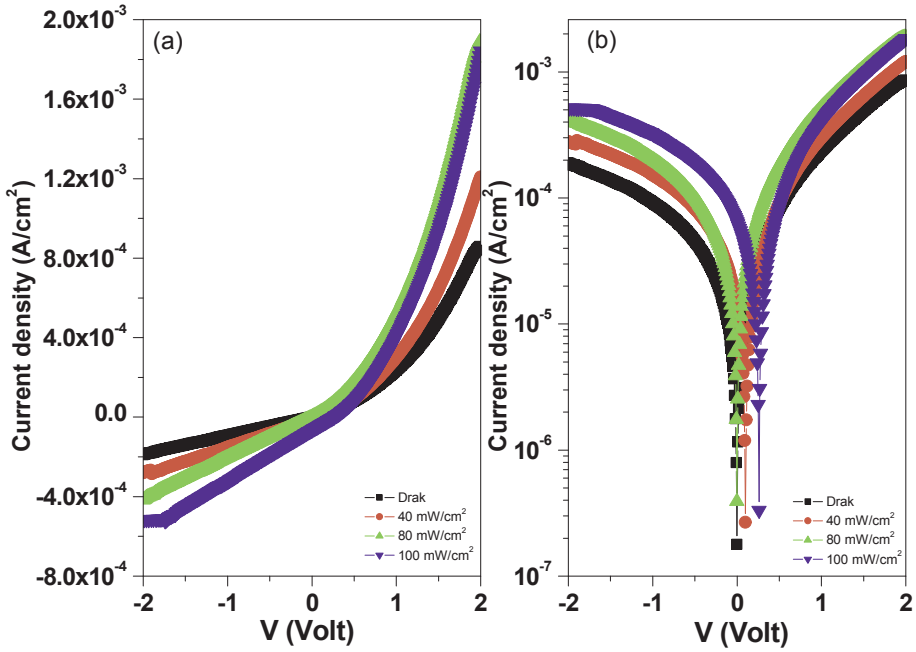

Fig. 9. (a) Current density-voltage characteristics, and (b) Semilogarithmic plot of Current density-voltage characteristics of **AMCMTT** thin films.

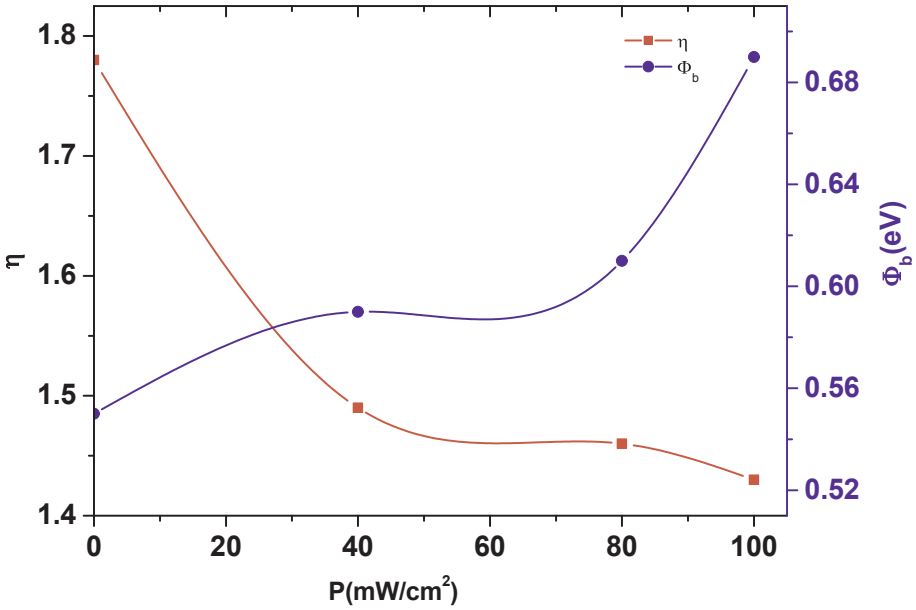

Fig. 10. Plot of η vs. P and Φ_b vs. P for **AMCMTT** thin films.

Table 2
The calculated current density-voltage characteristics of **MCMTT** based.

StateP (mW/cm^2)	R_s (kΩ)	R_{sh} (kΩ)	J_{sc} (A/cm^2)	V_{oc}(V)	FF
40	1.6	6.5	1.1×10^{-5}	0.08	0.28
80	1.1	4.8	3.0×10^{-5}	0.12	0.31
100	0.9	3.0	6.5×10^{-5}	0.23	0.27

increasing illumination intensity which can be interpreted to the enhancement of the photoconductivity characteristics of the heterojunction under influence of illumination, in agreement with the published results [45,46]. Using the results of Fig. 9(a), the part of the fourth quadrant is determined and illustrated in Fig. 11(a). The current-voltage characteristics under the reverse bias are highly affected by the influence of the illumination intensities as compared with those for the forward one confirming that the prepared heterojunction is adequate for the application of the photovoltaic and/or photodiode fields. The plot of the output power, P_{out} vs. V is depicted in Fig. 11(b). As observed, the output power P_{out} attains a maximum value at a certain applied bias depending on the illumination intensity. The calculated photovoltaic parameters are also represented as a function of illumination intensity and tabulated in Table 2. Besides, the other photovoltaic parameters like J_{sc} and V_{oc} are plotted as a function P (Fig. 12(a) and (b)) also listed in Table 2. As observed, the dependence of both the short-circuit current and the open-circuit voltage on P is detected with an exponential increase with the applied illuminations. Furthermore, the open circuit voltage reaches its maximum (0.23 V) at illumination intensity of 100 mW/cm^2. Moreover, the short-circuit current is found to increase with increasing the illumination intensities confirming the linearity for all the studied range of illumination. This illustration gives

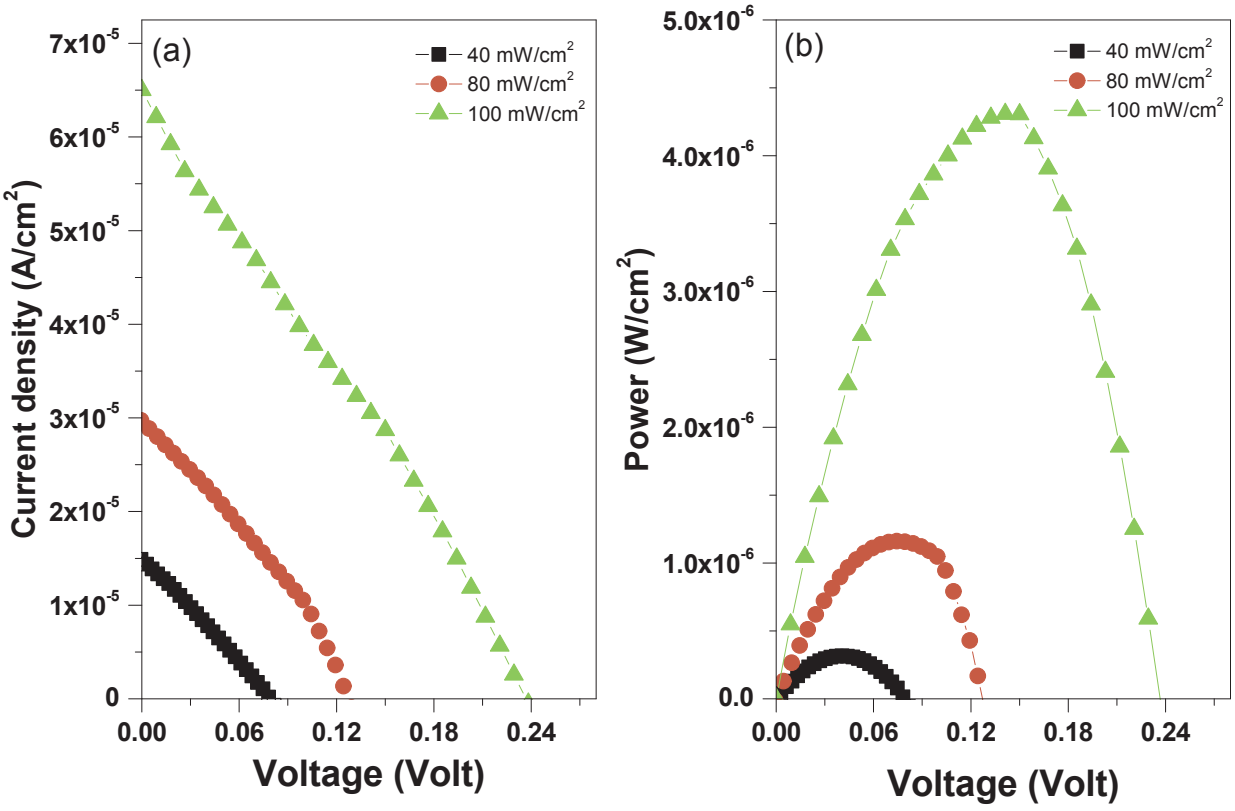

Fig. 11. (a) Plot of current density vs. voltage and (b) Power vs. voltage for **AMCMTT** thin films.

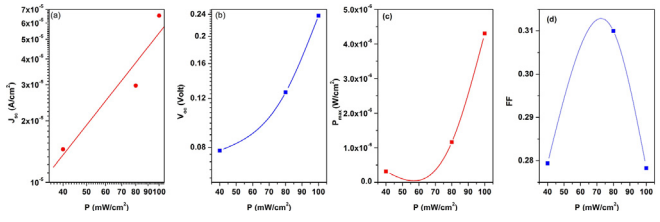

Fig. 12. (a) Plot of J_{sc} vs. P and (b) V_{oc} vs. P (c) Plot of P_{max}vs. P, and (d) FF vs. P for **AMCMTT** thin films.

a linear relation fit with a slope of 1.49. The high value of the slope suggests that the predominant conduction mechanism agrees with bi-molecular recombination and/or mono-molecular recombination and/or super linear recombination, respectively [47,48]. The obtained maximum power, P_{max} versus the illumination intensity, P (Fig. 12(c)) shows increasing of P_{max} with increasing illumination intensity as listed in Table 2. In addition, (Fig. 12(d)) the fill factor illustrates maximum value at illumination intensity of 70 mW/cm^2.

4. Conclusion

In conclusion, 4-{(2-amino-6-methylchromon-3-yl) methylidene] amino}-6-methyl-3-thioxo-3,4-dihydro-1,2,4-triazin-5(2*H*)-one (**AMCMTT**) has been successfully prepared and fully characterized. The optimized geometries of the structure were achieved using the B3LYB/6-311G (p, d) level.

The optical absorption characteristics in the UV–vis spectrum of **AMCMTT** shows four essential bands at 365.37 nm, 330.86 nm, 308.40 nm, 278.26 nm due to charge transfer, n→π*, π→π*, and π-π* transitions as reflected from their intensities, respectively. The 3D of the well-defined molecular electrostatic potentials were calculated and discussed. The obtained dispersion parameters of E_d and E_0 were found to be 3.984 and 2.04 eV, respectively. The optical properties were examined by means of the spectrophotometric method. The measured energy gaps were found to be directly allowed with energies of 1.00 and 2.76 eV.

The behavior of ideality factor and barrier height of the heterojunction-based AMCMTT under influence of illumination were attributed to the molecular modulation such as restructuring and reordering of the interface states, generation and recombination processes. In addition, the heterojunction exhibited photovoltaic properties with remarkable conversion power efficiency as compared with those for most organic-based devices. The obtained results of the heterojunction illumination dependence support the utilization of the AMCMTT-based device for photodiode applications.

Acknowledgment

The authors would like to thank Prof. A.Taha, Chemistry Department, Ain Shams University, for his scientific support.

References

[1] A. Gaspar, M.J. Matos, J. Garrido, E. Uriarte, F. Borges, Chromone: a valid scaffold in medicinal chemistry, Chem. Rev. 114 (2014) 4960–4992.
[2] Y.Q. Shi, T. Fukai, H. Sakagami, W.-J. Chang, P.Q. Yang, F.P. Wang, T. Nomura, Cytotoxic flavonoids with isoprenoid groups from Morus mongolica, J. Nat. Prod. 64 (2001) 181–188.
[3] P. Valenti, A. Bisi, A. Rampa, F. Belluti, S. Gobbi, A. Zampiron, M. Carrara, Synthesis and biological activity of some rigid analogues of flavone-8-acetic acid, Bioorg. Med. Chem. 8 (2000) 239–246.
[4] R. Larget, B. Lockhart, P. Renard, M. Largeron, A convenient extension of the Wessely–Moser rearrangement for the synthesis of substituted alkylaminoflavones as neuroprotective agents in vitro, Bioorg. Med. Chem. Lett. 10 (2000) 835–838.
[5] J. Ungwitayatorn, W. Samee, J. Pimthon, 3D-QSAR studies on chromone derivatives as HIV-1 protease inhibitors, J. Mol. Struct. 689 (2004) 99–106.
[6] H. Göker, D.W. Boykin, S. Yıldız, Synthesis and potent antimicrobial activity of some novel 2-phenyl or methyl-4H-1-benzopyran-4-ones carrying amidinobenzimidazoles, Bioorg. Med. Chem. 13 (2005) 1707–1714.
[7] P.J. Pietta, Flavonoids as antioxidants, J. Nat. Prod. 63 (2000) 1035–1042.
[8] U. Albrecht, M. Lalk, P. Langer, Synthesis and structure–activity relationships of 2-

vinylchroman-4-ones as potent antibiotic agents, Bioorg. Med. Chem. 13 (2005) 1531–1536.
[9] A. Nohara, T. Umetani, Y. Sanno, A. Nohara, T. Umetani, Y. Sanno, Studies on antianaphylactic agents—I: a facile synthesis of 4-oxo-4*H*-1-benzopyran-3-carboxaldehydes by Vilsmeier reagents, Tetrahedron 30 (1974) 3553–3556.
[10] M.A. Ibrahim, Studies on the chemical reactivity of 1H-benzimidazol-2-ylacetonitrile towards some 3-substituted chromones, Tetrahedron 69 (2013) 6861–6865.
[11] M.A. Ibrahim, Novel chromeno[2,3-b]pyridines from basic rearrangement of 4-oxochromene-3-carbonitrile, Synth. Commun. 39 (2009) 3527–3545.
[12] M.A. Ibrahim, N.M. El-Gohary, S. Said, S.S. Ibrahim, Synthesis of some novel heteroannelated chromones by basic rearrangement of 6-methylchromone-3-carbonitrile, Chem. Heterocycl. Compd. 50 (2015) 1624–1633.
[13] M.A. Ibrahim, N.M. El-Gohary, S. Said, Ring opening ring closure reactions with 3-substituted chromones and ER nucleophilic, Heterocycles 91 (2015) 1863–1903.
[14] U. Petersen, H. Heitzer, Reactions of 4-oxo-4H-chromene-3-carbaldehyde reactions, Liebigs Ann. Chem. 9 (1976) 1659–1662.
[15] A. Dornow, M.P. Menzel, Synthesen stickstoffhaltiger Heterocyclen, XXVII. Über 1.2. 4-Triazine, I Darstellung einiger neuer s-Triazolo [3.2-c]-as-triazine, Chem. Ber. 97 (1964) 2173–7278.
[16] (a) A.D. Becke, Density-functional thermochemistry. III. The role of exact exchange, J. Chem. Phys. 98 (1993) 5648–5652;
(b) A.D. Becke, Density-functional thermochemistry. I. The effect of the exchange-only gradient correction, J. Chem. Phys. 96 (1992) 2155–2160.
[17] (a) C. Lee, W. Yang, R.G. Parr, Development of the Colle-Salvetti correlationenergy formula into a functional of the electron density, Phys. Rev. B Condens. Matter 37 (1988) 785–789;
(b) B. Miehlich, A. Savin, H. Stolt, H. Preuss, Results obtained with the correlation energy density functionals of Becke and Lee, Yang and Parr, Chem. Phys. Lett. 157 (1989) 200–206.
[18] B.B. Stefanov, G. Liu, A. Liashenko, P. Piskorz, I. Komaromi, R.L. Martin, D.J. Fox, T. Keith, M.A. Al-Laham, C.Y. Peng, A. Nanayakkara, M. Challacombe, P.M.W. Gill, B. Johnson, W. Chen, M.W. Wong, C. Gonzalez, J.A. Pople, Gaussian, Inc., Pittsburgh PA, 2003.
[19] M.J. Frisch, G.W. Trucks, H.B. Schlegel, G.E. Scuseria, et al., Gaussian, Inc., Wallingford CT, 2009.
[20] R. Dennington, T. Keith, J. Millam, GaussView, Version 5, Semichem Inc., Shawnee Mission KS, 2009.
[21] http://www.chemcraftprog.com.
[22] N.V. Kulkarni, N.H. Bevinahalli, V.K. Revankar, J. Coord. Chem. 63 (2010) 1785–1789.
[23] M.A. Ibrahim, A.A.M. Farag, N. Roushdy, N.M. El-Gohary, Synthesis, optical and photoelectrical characterizations of the novel 10-chloro-6H,8H-dichromeno[2,3-b:3′,4′-e]pyridine-6,8-dione (CDPD) and its photodiode application, Opt. Mater. 51 (2016) 70–77.
[24] Shimaa Abdel Halim, Magdy A. Ibrahim, Synthesis, DFT calculations, electronic structure, electronic absorption spectra, natural bond orbital (NBO) and nonlinear optical (NLO) analysis of the novel 5-methyl 8Hbenzo[h]chromeno[2,3-b][1,6] naphthyridine-6(5H),8-dione (MBCND), J. Mol. Str. 1130 (2017) 543–558.
[25] J.B. Lambert, H.F. Shurvell, L. Vereit, R.G. Cooks, G.H. Stout, Organic Structural Analysis, Academic Press, New York, 1976.
[26] P.S. Kalsi, Spectroscopy of Organic Compounds, Academic Press, New York, 2002.
[27] R.M. Bassler, G.C., T.C. Morrill, Spectrometric Identification of Organic Compounds, fourth ed., John Wiley and Sons, New York, 1981.
[28] A. Prakasam, V. Sakthi, X.,P.M. Anbarasan, DFT studies on the electronic structures of 4 methoxybenzonitrile dye for dye-sensitized solar cell, Int. Lett. Chem. Phys. Astron. 7 (2013) 8–22.
[29] M. Drissi, N. Benhalima, Y. Megrouss, R. Rachida, A. Chouaih, F. Hamzaoui, Theoretical and experimental electrostatic potential around the m-nitrophenol molecule, Molecules 20 (2015) 4042–4054.
[30] R. Kaur, P. Singh, K. Singh, A. Kumar, A. Thakur, Optical band gap tuning of Sb-Se thin films for xerographic based applications, Superlattice. Microstruct. 98 (2016) 187–193.
[31] P. Jayaprakash, M.P. Mohamed, M.L. Caroline, Growth and characterization of l-asparagine monohydrate admixtured dl-mandelic acid nonlinear optical single crystal, J. Mol. Str. 1134 (2017) 67–77.
[32] J. Bardeen, F.J. Blatt, L.H. Hall, Photoconductivity Conference, Wiley, NewYork, 1956.
[33] P. Lazic, R. Armiento, F.W. Herbert, R. Chakraborty, R. Sun, M.K.Y. Chan, K. Hartman, T. Buonassisi, B. Yildiz, G. Ceder, J. Phys. Condens. Matter 25 (2013) 465801.
[34] Magdy A. Ibrahim, Shimaa Abdel Halim, N. Roushdy, A.A.M. Farag, Nasser M. El-Gohary, Synthesis, DFT study and photoelectrical characterizations of the novel 4-methoxyfuro[3‘,2‘:6,7]chromeno[2,3- e]benzo[b][1,4]diazepin-5(12H)-one, Optik 166 (2018) 294–306.
[35] S.H. Wemple, M. DiDomenico, Behavior of the electronic dielectric constant in covalent and ionic materials, Phys. Rev. B 3 (1971) 1338–1351.
[36] E.D. Palik, Handbook of Optical Constants of Solids, Academic Press Handbook, New York, 1985.
[37] M.S. El-Bana, S.S. Fouad, Optoelectrical properties of $Ge_{10}Se_{90}$ and $Ge_{10}Se_{85}Cu_5$ thin films illuminated by laser beams, J. Alloys Compd. 695 (2017) 1532–1538.
[38] U. Zhokhavets, R. Goldhahn, G. Gobsch, W. Schliefke, Dielectric function and one-dimensional description of the absorption of poly(3-octylthiophene), Synth. Met. 138 (2003) 491–495.
[39] Y.Q. Xue, M.A. Ratner, Microscopic study of electrical transport through individual molecules with metallic contacts, Phys. Rev. B 68 (2003) 115407.
[40] H.G. Cetinkay, H. Tecimer, H. Uslu, S. Altındal, Photovoltaic characteristics of Au/PVA (Bi-doped)/n-Si Schottky barrier diodes (SBDs) at various temperatures, Curr. Appl. Phys. 13 (2013) 1150–1156.
[41] H. Norde, A modified forward I-V plot for Schottky diodes with high series resistance, J. Appl. Phys. 50 (1979) 5052–5053.
[42] S.K. Cheung, N.W. Cheung, Extraction of Schottky diode parameters from forward current-voltage characteristics, Appl. Phys. Lett. 49 (1986) 85–87.
[43] E.H. Nicollian, J.R. Brews, MOS Phys. Tech. Wiley, New York, 1982.
[44] S. Aydogan, K. Cınar, H. Asıl, C. Coskun, A. Turut, Electrical characterization of Au/n-ZnO Schottky contacts on n-Si, J. Alloys Compd. 476 (2009) 913–918.
[45] I.S. Yahia, F. Yakuphanoglu, S. Chusnutdinow, T. Wojtowicz, G. Karczewski, Photovoltaic characterization of n-CdTe/p-CdMnTe/GaAs diluted magnetic diode, Curr. Appl. Phys. 13 (2013) 537–543.
[46] R.H. Bube, Photoconductivity of Solids, Wiley, New York, 1960.
[47] A. Rose, Concepts in Photoconductivity, Interscience, New York, 1960.
[48] V.M. Nikale, S.S. Shinde, A.R. Babar, C.H. Bhosale, K.Y. Rajpure, Photoelectrochemical performance of sprayed n-$CdIn_2Se_4$ photoanodes, Sol. Energy 85 (2011) 325–333.